Journal of Catalysis 266 (2009) 380–390

Contents lists available at ScienceDirect

Journal of Catalysis

journal homepage: www.elsevier.com/locate/jcat

MCM-41 supported nickel-based bimetallic catalysts with superior stability during carbon dioxide reforming of methane: Effect of strong metal–support interaction

Dapeng Liu [a], Xian Yang Quek [a], Wei Ni Evelyn Cheo [a], Raymond Lau [a], Armando Borgna [b], Yanhui Yang [a,*]

[a] School of Chemical and Biomedical Engineering, Nanyang Technological University, Singapore 637459, Singapore
[b] Institute of Chemical and Engineering Sciences (ICES), A*STAR, 1 Pesek Road, Jurong Island, Singapore 627833, Singapore

ARTICLE INFO

Article history:
Received 24 March 2009
Revised 3 July 2009
Accepted 8 July 2009
Available online 7 August 2009

Keywords:
Methane dry reforming
Nickel bimetallic catalyst
MCM-41
Anchoring effect
Decoration effect

ABSTRACT

Nickel-based bimetallic catalysts supported on MCM-41 mesoporous molecular sieves (Ni–Ti-, Ni–Mn-, and Ni–Zr–MCM-41) were prepared by direct hydrothermal synthesis. The catalytic properties were tested in methane reforming with CO_2. All Zr-promoted catalysts exhibited comparable or enhanced initial catalytic activity as compared to Ni–MCM-41. Adding Zr^{4+} remarkably improved the long-term stability, whereas decreased lower initial activity and stability were observed for Ti- and Mn-modified catalysts. The addition of Zr^{4+} enhanced the structural stability and the dispersion of active Ni sites. The strong anchoring effect of Zr^{4+} and the partial activation of CO_2 by Zr^{4+} contributed to the high catalytic activity and long-term stability. On the contrary, the decoration of Ni clusters with TiO_x and MnO_x species on Ni–Ti and Ni–Mn catalysts hindered the accessibility of Ni-active centers, thus decreasing their catalytic performance. The partial transformation of amorphous silica matrix into quartz and/or tridymite phases over Ni–Mn, Ni–Ti, and Ni–MCM-41 catalysts also played a negative role on their catalytic stability.

1. Introduction

Recently, the production of synthesis gas (syngas) via carbon dioxide dry reforming has received renewed attention due to environmental concerns and the clear need to reduce GHGs (Green House Gases) emissions. The syngas produced by dry reforming has a lower H_2/CO ratio, being preferred for the production of valuable oxygenated chemicals and long chain hydrocarbons [1,2]. Dry reforming can also be utilized in chemical energy transmission systems (CETS) based on the high endothermicity of this reaction [3]. However, a major challenge that hinders the development of dry reforming process is the lack of an effective catalyst, able to operate efficiently under severe reaction conditions with good stability.

Both noble metal (Rh, Ru, Pt, and Pd) and non-noble metal (Fe, Co, and Ni) catalysts have been investigated [4,5]. Nickel is considered as a good replacement for noble metal due to its comparable catalytic performance and low cost. However, nickel-based catalysts are well known for their high tendency to carbon deposition [6,7]. Besides coking, the deactivation of reforming catalyst can also be associated with the sintering of metal clusters [8,9] and/or the structural stability of the catalysts [10–12]. Under industrial high pressure conditions needed for attaining high productivity, the use of membrane reactors was suggested to be a promising approach since the removal of hydrogen from the reaction mixture by preferential permeation can drive the reaction forward and prevent any further reaction of hydrogen with other components [13,14]. A fundamental problem that has been identified is the conversion of hydrogen into water through reverse water gas shift reaction (RWGS) and, currently, there is no solution for this drawback [13]. However, the development of suitable catalysts to promote the conversion of reactants while maintaining well-dispersed active sites and exhibiting good structural stability still remains a challenge.

Significant efforts were devoted to improve the catalytic properties of nickel-based catalysts. In conventional steam reforming, e.g., SPARG process, Sulfur PAssivated ReforminG process, carbon deposition can be reduced by partially sulfur poisoning the catalyst since sulfur can preferentially eliminate the large nickel ensembles that promote nucleation of carbon [15]. However, sulfur passivation remarkably lowers the catalytic activity and leads to the presence of traces of sulfur in the syngas. It has been reported that basic oxides or basic promoters can be an efficient way for reducing carbon formation during dry reforming on nickel-based

* Corresponding author. Fax: +65 6794 7553.
E-mail address: yhyang@ntu.edu.sg (Y. Yang).

0021-9517/$ - see front matter © 2009 Elsevier Inc. All rights reserved.
doi:10.1016/j.jcat.2009.07.004

catalysts. Ruckenstein and Hu reported that reduced NiO/MgO catalysts exhibit high activity and stability since the formation of NiO–MgO solid solution controls the nickel cluster size, thereby inhibiting the carbon deposition efficiently [16]. Particularly, the increase in basicity strengths the CO_2 adsorption, thus reducing carbon formation considerably [17–19]. The high reaction rate and stability over Ni/La_2O_3 catalyst were closely associated with the partial coverage of Ni particles by $La_2O_2CO_3$ species, leading to a significant increase in coking resistance due to a synergetic effect [19]. Depending on the preparation method and catalyst composition, high catalytic activity and low carbon deposits are also observed on Ni/ZrO_2 catalysts [20,21].

The influence of introducing a second metal on nickel catalysts was also investigated. A decrease in carbon deposition was found on $Ni/MnO–Al_2O_3$ catalyst during reforming. This was attributed to the partial coverage of nickel surface by MnO_x patches, affecting CO_2 adsorption [22]. A beneficial effect of Cr on the catalytic activity was observed over Ni–Cr/yttria-doped ceria (YDC) catalyst by Wang et al. [23], where the surface oxygen vacancies of YDC also played an important role in stabilizing the bimetallic Ni–Cr catalysts. Recently, a series of Ni–Me–Al–Mg–O composite catalysts (Me = Co, Fe, Cu, or Mn) have been investigated by Zhang et al. [24]. It was reported that Ni–Co bimetallic catalyst had a superior catalytic performance as compared to other Ni–Me combinations. This superior performance was ascribed to the high metal dispersion, strong metal–support interaction, and the formation of stable solid solutions. However, other authors reported a negative effect on the catalytic performance over nickel catalysts modified by Fe, Co, Cu Ce, and Mo [25,26].

Mesoporous molecular sieves MCM-41, one of the M41S family members developed by Mobil Oil Corporation scientists, has attracted considerable and continuously growing interest since its discovery in 1992 [27,28]. The striking properties such as high specific surface area, regular nano-sized pore structure, and adjustable heteroatom compositions enable these materials to be widely used as adsorbents, catalyst supports, and heterogeneous catalysts [29]. The incorporation of active metals into the framework of MCM-41 molecular sieves makes them particularly valuable for catalytic applications. During the partial oxidation of methane to formaldehyde, a high HCHO selectivity of ca. 60% was achieved over V–MCM-41 catalyst [30]. The enhanced catalytic performance of the V–MCM-41 catalysts was attributed to the highly dispersed vanadium oxide species, minimizing the consecutive oxidation of formaldehyde. Almost 100% selectivity toward methane was reported for CO_2 methanation over nickel-incorporated MCM-41 catalyst, which was superior to that of Ni/SiO_2 catalysts and comparable to the performance of Ru/SiO_2 catalysts [31]. The superior performance was ascribed to the formation of highly dispersed Ni particles. In our previous work [32], a highly ordered Ni-substituted MCMC-41 catalyst was developed, showing remarkably improved catalytic activity and stability during dry reforming as compared to supported nickel catalysts obtained by wet impregnation. The improved catalytic performance of Ni–MCM-41 was attributed to the anchoring effect of nickel-active sites by the peripheral silica matrix and/or the unreduced nickel ions. The enhancement of the catalytic performance and stability after pretreating the Ni–MCM-41 samples under inert gases were also reported [32].

In the present contribution, we extend the investigation to nickel-based bimetallic mesoporous MCM-41 catalysts for CO_2 dry reforming. The catalysts were prepared by direct incorporation of nickel along with titanium, manganese, or zirconium ions into the silica framework. The second transition metal ions are suggested to affect the catalytic performances of nickel-based MCM-41 catalysts due to the strong interaction between metal and support.

2. Experimental

2.1. Catalyst preparation

Mono- and bi-metallic incorporated mesoporous MCM-41 catalysts were prepared following the procedure described elsewhere [33]. Nickel nitrate ($Ni(NO_3)_2{\cdot}6H_2O$), titanium *n*-butoxide (TBOT, $Ti(OC_4H_9)_4$), manganese acetate ($Mn(CH_3COO)_2{\cdot}4H_2O$), and zirconyl nitrate ($ZrO(NO_3)_2{\cdot}xH_2O$) were used as metal precursors. Fumed silica (Cab-O-Sil, SiO_2), tetramethyl ammonium silicate ($((CH_3)_4N(OH){\cdot}2SiO_2$), and sodium silicate ($Na_2Si_3O_7$) were selected as silica sources. Cetyltrimethylammonium bromide (CTAB, $C_{16}H_{33}(CH_3)_3NBr$) was used as structure-directing agent. The molar composition of the resulting gel was $1.0SiO_2$:*x*Ni:*y*M:0.28CTAB:60-H_2O (M = Ti, Mn, or Zr). For titanium-containing sample, a small amount of isopropanol (IPA) was used to dissolve TBOT with a molar ratio of IPA/TBOT = 85 during gel preparation to prevent the rapid hydrolysis of the Ti source. The resulting gels were crystallized in a Teflon-lined autoclave at 120 °C for 3 days under autogenous pressure. The solids were recovered by filtration, washed with deionized water, and dried at ambient temperature over night. The template was removed by calcination at 540 °C for 6 h.

2.2. Characterization of catalysts

X-ray diffraction (XRD) measurements were carried out on a Bruker AXS D8Focus diffractometer using Ni-filtered Cu Kα radiation (λ = 0.15406 nm), operated at 40 kV and 40 mA. The average crystallite size of metallic Ni in the spent catalysts was calculated using the Scherrer equation. Nitrogen adsorption–desorption isotherms were measured at −196 °C on a Quantachrome AUTOSORB-6B static volumetric instrument. Prior to the measurements, the samples were degassed at 280 °C for 5 h under high vacuum. The specific surface areas were calculated using the BET method [34] and the pore size distributions were estimated by the BJH method [35], using the desorption branch. UV–Vis spectra in the range of 190–800 nm were measured with a Varian Cary 5000 UV–Vis–NIR spectrophotometer equipped with a diffuse-reflectance accessory at ambient temperature. The reducibility of catalysts was studied by hydrogen temperature-programed reduction (TPR) on a Quantachrome AUTOSORB-1C apparatus. Before reduction, the samples were pretreated with air at 500 °C for 60 min and then cooled down to 90 °C. All TPR runs were performed from 90 to 900 °C under 5% H_2 in Ar with a heating rate of 8 °C/min. The consumption of hydrogen was monitored on-line with a built-in thermal conductivity detector (TCD).

Carbon formation was quantitatively analyzed on a Perkin–Elmer Pyris Diamond TG/DTA instrument under air atmosphere using a heating rate of 10 °C/min within a temperature range of 30–800 °C. Laser-Raman spectra were recorded in the range of 1000–2000 cm^{-1} using a laser excitation wavelength of 633 nm on a Renishaw Raman spectrometer with a Nd:YAG laser source under ambient condition. Transmission electron microscopy (TEM) image was obtained on a JEOL JEM-1400 microscope operated at 120 kV. The samples were prepared by dispersing the spent catalyst powder in ethanol using ultrasound, and then deposited and dried on holey carbon-coated Cu grids. Hydrogen chemisorption was performed in a conventional static volume apparatus (Quantachrome AUTOSORB-1C). The samples were first dried under He atmosphere at 250 °C for 2 h and reduced in purified H_2 at 750 °C for 2 h using a heating rate of 5 °C/min. The samples were evacuated at this temperature for 2 h, and then cooled down in vacuum to 40 °C for the chemisorption measurement. The hydrogen monolayer uptake of the catalysts was calculated by extrapolating the isotherm to zero pressure. An adsorption stoichiometry

of one hydrogen adsorbed per surface Ni atom was assumed. The Ni particle size was calculated using the formula, $d_{Ni} = 6V/S$, where V is the volume of total metallic Ni and S is the active Ni surface area assuming the Ni particles were spherical in shape. The percentage of Ni dispersion was calculated by dividing the number of exposed surface Ni atoms (determined by H_2 chemisorption) by the total number of Ni atoms in the catalyst.

2.3. Catalytic experiments

Activity tests were performed under atmospheric pressure in a continuous down flow quartz fixed-bed reactor. Typically, 0.12 g of catalyst was loaded in the reactor using quartz wool. A feed with a constant CH_4/CO_2/He molar ratio of 1:1:2 was used in all experiments. The space velocity of the total gas mixture was fixed at 50,000 mL/h gCat. The initial activity was measured from 600 to 800 °C in steps of 50 °C, using a step duration 30 min. For the stability tests, the reaction temperature was kept constant at 750 °C for 30 h on stream (TOS). Prior to each test, the catalysts were pretreated in situ at 750 °C for 2 h under He. The composition of the reaction products was analyzed using an on-line gas chromatograph (Agilent 6890) equipped with a Porapak Q column and a TCD. The conversions of CH_4 and CO_2, the selectivities of H_2 and CO and the ratio of CO/H_2 were calculated as previously reported [32].

3. Results and discussion

3.1. Physicochemical properties of the catalysts

Small-angle XRD patterns of all calcined catalysts (Fig. 1A) shows one major (100) reflection, along with two minor reflections corresponding to the (110) and (200) planes, indicating a highly ordered hexagonal pore structure. No diffraction peak is observed at a high angle range for calcined catalyst (not shown here), implying that most of the metal ions have been inserted into the silica framework or are highly dispersed on the silica pore wall surface. The diffraction peaks become broader and less intense upon introducing the second metal because the substitution of Si^{4+} by metal ions results in an alteration of the T–O–T bond angle and a slight decrease in the long range order of the mesostructures. Nitrogen physisorption data of calcined catalysts (Fig. 1B) shows type IV isotherms with a sharp increase of nitrogen uptake at the intermediate relative pressures, which is caused by capillary condensation of nitrogen inside the mesopores [36]. After the mesopores are filled, the adsorption and desorption isotherms become flat, indicating that the external surface area of MCM-41 catalysts is small. A small hysteresis loop at relative pressures above 0.9 is ascribed to the condensation of nitrogen within the interstitial voids created by MCM-41 particles.

Textural parameters of calcined Ni-based MCM-41 catalysts are summarized in Table 1. These materials exhibit a unit cell parameter (a_0) within the range of 4.2–4.4 nm, depending on the amount and type of metal cations introduced into the MCM framework. The expansion of a_0 for these nickel-based catalysts as compared to that of pure siliceous MCM-41 (a_0 = 3.8 nm) indicates the incorporation of metal cations into the silica framework. This is also in agreement with the absence of crystalline phases of metal oxides in the XRD diffraction patterns at high angles. All samples possess high surface areas, typically larger than 900 m^2/g. The isomorphous substitution of silicon with a small amount of Ni, Ti, Mn, or Zr has a little effect on the pore diameter. Moreover, the wall thickness is comparable for all samples.

UV–Vis spectroscopy has been extensively used to characterize the nature and coordination structure of various transition metal ions. Fig. 2 shows the UV–Vis spectra of metal-incorporated MCM-41 samples along with NiO spectrum, taken as reference. An intense and broad band at 259 nm and several weak adsorptions at 381, 411, 550, and 718 nm for NiO reference sample are observed, suggesting that Ni^{2+} ions are in an octahedral local environment [37,38]. The above main bands are absent for all the nickel-incorporated MCM-41 samples while only a weak band at around 400 nm can be discerned, implying that most of the Ni species in these MCM-41 materials exist in a distorted tetrahedral environment. Over 2Ni–2Zr, this 400 nm band shifts to 417 nm and becomes more intense, suggesting that the change of the Ni^{2+} local symmetry probably occurs in the presence of Zr^{4+}. For all Ni–Zr samples, one single narrow band at about 200 nm is ob-

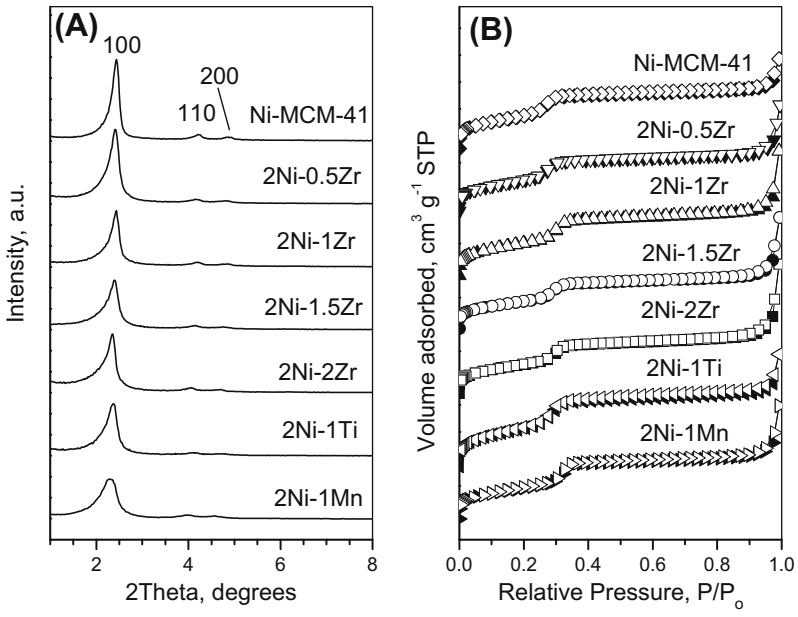

Fig. 1. XRD patterns (A) and nitrogen physisorption results (B) of representative Ni-containing bimetallic MCM-41 samples: 2Ni–1Mn, 2Ni–1Ti, 2Ni–2Zr, 2Ni–1.5Zr, 2Ni–1Zr, 2Ni–0.5Zr, and Ni–MCM-41 (from bottom to top).

Table 1
Textural characteristics of various Ni-containing MCM-41 samples.

Sample ID	Metal content[a] (wt.%)		Unit cell (nm)[b]	Surface area (m^2/g)	Pore size (nm)	Pore wall thickness[c] (nm)
	Ni	M[d]				
Ni–MCM-41	2.00	0	4.2	1078	2.5	1.7
2Ni–0.5Zr	1.98	0.48	4.2	1019	2.5	1.7
2Ni–1Zr	1.93	0.92	4.2	1077	2.5	1.7
2Ni–1.5Zr	1.92	1.45	4.3	910	2.5	1.8
2Ni–2Zr	1.88	1.85	4.3	974	2.5	1.8
2Ni–1Ti	1.95	0.88	4.3	1261	2.5	1.8
2Ni–1Mn	1.92	0.93	4.4	1024	2.7	1.7

[a] Metal content designates the nominal metal loading.
[b] The unit cell parameter a_0 was calculated from $a_0 = 2d_{100}/\sqrt{3}$.
[c] Wall thickness was determined by the difference between unit cell parameter and pore size.
[d] M denotes the second metal.

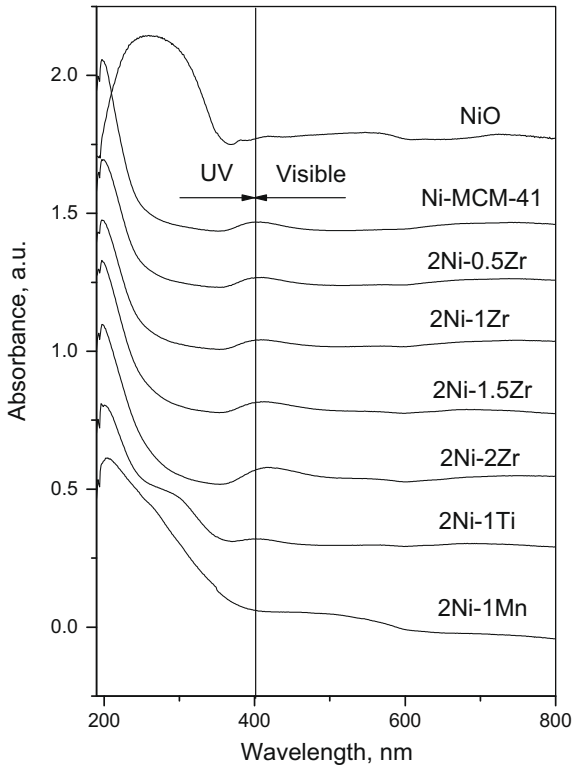

Fig. 2. UV–Vis spectra of various samples: NiO reference, Ni–MCM-41, 2Ni–0.5Zr, 2Ni–1Zr, 2Ni–1.5Zr, 2Ni–2Zr, 2Ni–1Ti, and 2Ni–1Mn.

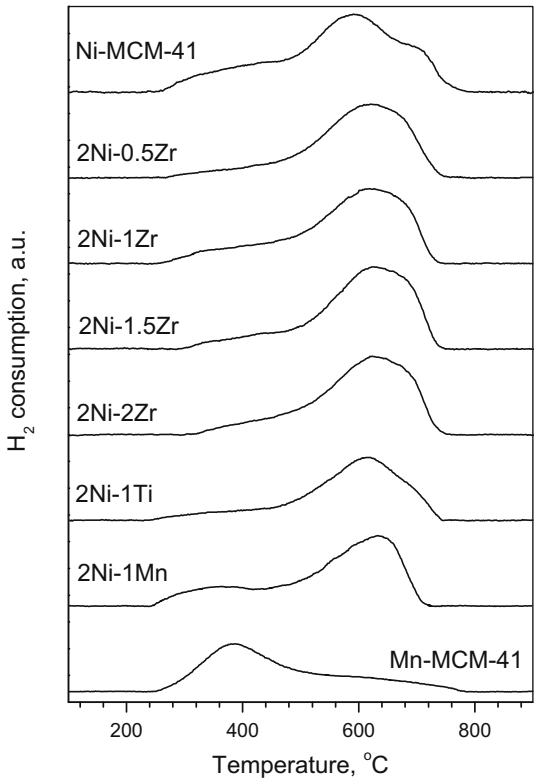

Fig. 3. TPR profiles of various samples: Ni–MCM-41, 2Ni–0.5Zr, 2Ni–1Zr, 2Ni–1.5Zr, 2Ni–2Zr, 2Ni–1Ti, 2Ni–1Mn, and Mn–MCM-41.

served, which can be attributed to the $O^{2-} \rightarrow Zr^{4+}$ charge-transfer transition with isolated Zr^{4+} in a tetrahedral coordination environment and the absence of ZrO_2 species inside the mesopores [39]. For the 2Ni–1Ti sample, the strong adsorption band below 250 nm suggests the presence of the distorted tetrahedral Ti species [40]. A small shoulder at around 293 nm can be assigned to penta- or octahedral coordinated Ti species, resulting from the interaction of Ti species with Ni species [41,42]. 2Ni–1Mn exhibits a broad and asymmetric band with peak at around 204 nm in the UV region along with a weak signal at about 500 nm. It can be assumed that both tetrahedral and octahedral Mn^{3+} species co-exist over 2Ni–1Mn, according to previous reported assignments of Mn^{3+} in tetrahedral coordination at 270 nm [43] and in octahedral coordination at 320 nm [44], respectively.

TPR profiles of various MCM-41 catalysts are displayed in Fig. 3. For the Mn–MCM-41 sample, one main reduction peak and a small shoulder are observed at around 386 and 565 °C, respectively. Due to the non-stoichiometric properties of manganese oxides, the assignment of the reduction peaks to specific Mn species is difficult. According to the previous reports [43,45], the first main peak can be ascribed to the reduction of surface MnO_x species into Mn^{3+} or Mn^{4+}. The shoulder can be mainly attributed to the reduction of Mn^{3+} ions inside the silica matrix. Considering the absence of the diffraction peaks of the MnO_x species in the XRD patterns, it can be suggested that a strong interaction between MnO_x and silica matrix exists because of most of the Mn^{3+} or Mn^{2+} cations are either incorporated into the silica framework or highly dispersed on the silica walls. Over the Ni–MCM-41 sample, one main reduction peak and two shoulders are found, which are related to the different locations of Ni ions; either dispersed on the subsurface or located in the silica framework [46,47]. No reduction peak was observed over Ti–MCM-41 and Zr–MCM-41 samples within the temperature range of the TPR tests.

Due to the introduction of the second metal, some changes of reduction patterns are expected for the bimetallic MCM-41 catalysts. For the 2Ni–1Mn sample, a shoulder and a main peak are observed at 353 and 630 °C, respectively. The shoulder could be probably due to the reduction of MnO_x, which is consistent with the TPR profile of Mn–MCM-41. The major peak is tentatively assigned to the reduction of Ni^{2+} in the silica framework, although the reduction of a small amount of incorporated Mn^{3+} species cannot be excluded. In the case of 2Ni–1Ti catalyst, an intense reduction peak at 617 °C along with a shoulder at around 420 °C are observed. The shoulder and the main reduction peak can be attributed to the reduction of Ni^{2+} ions. A broad reduction peak reflects the different locations of Ni^{2+} ions. It is important to mention that the partial reduction of the incorporated Ti^{4+} to Ti^{3+} at 617 °C is unavoidable, which is most likely induced by hydrogen spillover effect. Therefore, it is suggested that the formation of Ni–TiO_x ($x < 2$) species may occur under high temperature reduction in this particular sample. A similar inductive reduction of Ti^{4+} ions was also found in Fe–Ti–MCM-41 sample because of the reduction of Fe^{3+} and Fe^{2+} [48]. All Ni–Zr catalysts exhibit similar reduction patterns, exhibiting an intense peak at around 600–660 °C, which is mainly originated from the reduction of the incorporated Ni^{2+} ions.

The active metal surface area, metal dispersion, and particle size of various Ni-containing MCM-41 are summarized in Table 2. As compared to the Ni–MCM-41 mono-metallic catalyst, an increase in active metal surface area and dispersion along with a decrease in metal particle size are observed with the incorporation of Zr into the MCM-41 framework. The greatest metal dispersion occurs over 2Ni–1Zr catalyst, followed by 2Ni–1.5Zr, 2Ni–0.5Zr, 2Ni–2Zr, and Ni–MCM-41. On the contrary, the metal surface area and dispersion are dramatically reduced for 2Ni–1Ti and 2Ni–1Mn catalysts. For the Ti-modified catalyst, a significant reduction of both active metal surface area and dispersion is expected since TiO_x patches can migrate onto the metal surface, covering the accessible Ni-active sites [49,50]. Similarly, the decrease in H_2 chemisorption capacity for the Mn-modified catalyst can be attributed to the facile reduction of MnO_x, partially covering the Ni particles.

3.2. Comparison of initial catalytic activity

Blank test showed a negligible catalytic activity under the reaction condition used in this contribution. The initial catalytic activities of various Ni-based catalysts were studied in the temperature range of 600–800 °C (Fig. 4). The CO/H_2 ratios are also included in Fig. 4. A remarkably higher catalytic conversion is observed over Ni–Zr- and Ni–MCM-41 catalysts than that of 2Ni–1Ti and 2Ni–1Mn. In fact, 2Ni–1Mn shows almost no activity while 2Ni–1Ti exhibits a relatively quite low activity, slightly higher at 750 °C. After 750 °C, the activity significantly decreases. 2Ni–1Zr shows the best catalytic performance among all Ni–Zr–MCM-41 catalysts. The considerably low catalytic activity of Mn- and Ti-modified catalysts suggests that the amount of available active sites on 2Ni–1Ti and 2Ni–1Mn samples is limited. Irrespective of 2Ni–1Ti and 2Ni–1Mn catalysts, the product CO/H_2 molar ratio decreases with reaction temperature (shown in Fig. 4B) and it approaches to 1 when the temperature is above 750 °C, in good agreement with previous report [51]. Low CH_4 conversion gives high CO/H_2 molar ratio because of the simultaneous presence of the RWGS reaction at low temperature. However, the explanation of the odd CO/H_2 ratio over 2Ni–1Ti and 2Ni–1Mn remains unclear. In summary, the substantial difference in both initial activity and CO/H_2 ratio between Zr-promoted and other transition metal-incorporated catalysts clearly indicates the beneficial effect of Zr substitution.

3.3. Comparison of long-term stability

The long-term stability evaluation of the catalysts was conducted at 750 °C, aiming to examine the effect of the incorporation of the second transition metal on the catalytic stability. The CH_4 conversions and the CO/H_2 molar ratios at 750 °C are presented in Fig. 5. Ti- and Mn-modified catalysts present extremely low CH_4 conversion in comparison with Ni–Zr series and non-modified Ni–MCM-41catalysts, which is consistent with the initial catalytic activity experiments at increasing temperature discussed above. After 2 h on stream, both Ti- and Mn-modified catalysts show a significant catalytic activity loss in CO_2 reforming, exhibiting CH_4 conversion lower than 4% (see Fig. 5A inset). On the contrary, all the Ni–Zr catalysts show enhanced catalytic stability, regardless of the amount of Zr introduced. No significant activity loss is found for 2Ni–1Zr, 2Ni–1.5Zr, and 2Ni–2Zr after 72 h on stream. For the highly active catalysts, the sequence of the catalytic stability is as follows: 2Ni–1Zr > 2Ni–1.5Zr ∼ 2Ni–2Zr > 2Ni–0.5Zr > Ni–MCM-41. As shown in Fig. 5B, all Ni-containing MCM-41 catalysts give a CO/H_2 molar ratio between 0.9 and 1.2, except for 2Ni–1Ti and 2Ni–1Mn. The poor catalytic activity and the unexpected product selectivity of the Ti- and Mn-modified samples may reflect the lack of accessible active centers for dry reforming.

3.4. Analysis of catalyst deactivation

In contrast to steam reforming, CO_2 reforming of CH_4 is more prone to form carbon deposition due to the absence of H_2O and the low H/C ratio in the feed. The deactivation of the supported catalysts by carbon formation is one of the serious obstacles for the practical application of this process [5]. Generally, two main pathways leading to carbon deposition have been proposed: CH_4 decomposition ($CH_4 \rightarrow C + 2H_2$) and CO disproportionation ($2CO \rightarrow C + CO_2$), also known as the Boudouard reaction. Besides carbon deposition, the sintering of metal particles under reaction condition and the structural stability of the catalysts are also

Table 2
Metal surface area, dispersion, and particle size of various Ni-containing MCM-41 samples.

Sample	Metal surface area (m^2/g)	Dispersion[a] (%)	Metal particle size[b] (nm)	
			D1[c]	D2[c]
Ni–MCM-41	0.69	5.2	19.5	27
2Ni–0.5Zr	0.81	6.2	16.2	24
2Ni–1Zr	0.87	6.6	15.4	21
2Ni–1.5Zr	0.84	6.3	16.0	25
2Ni–2Zr	0.77	5.8	17.6	25
2Ni–1Ti	0.19	1.4	49.8	21
2Ni–1Mn	0.32	2.9	33.0	16

[a] Dispersion is calculated assuming $H_{ad}/Ni_{surf} = 1$.
[b] Metal particle shape is assumed to be spherical.
[c] D1 denotes metal particle size of the reduced samples determined by chemisorption while D2 designates the particle size of the used catalysts after stability evaluation measured by XRD.

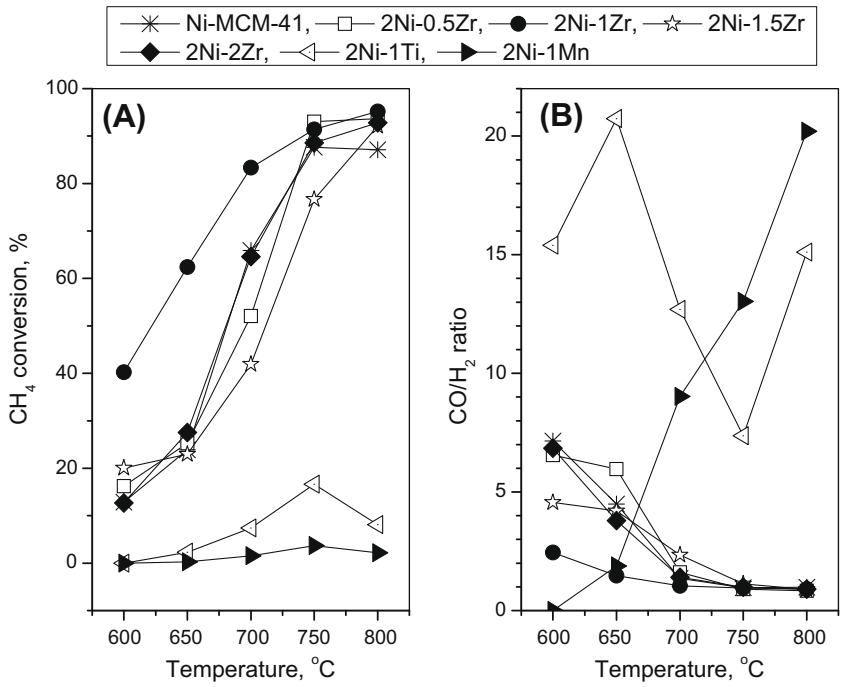

Fig. 4. Effect of reaction temperature on catalytic activities (A) and CO/H_2 ratio (B) over Ni-containing MCM-41 samples. Reaction conditions: WHSV (mL/h gCat) = 50,000, $CH_4/CO_2/He$ = 1:1:2, temperature range = 600–800 °C, P = 1 atm.

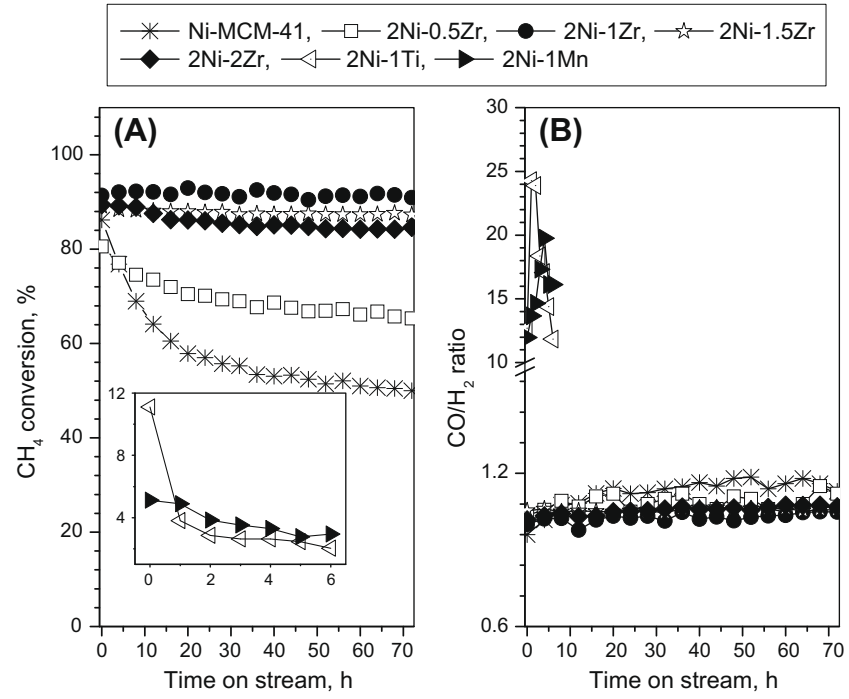

Fig. 5. Catalytic stability (A) and CO/H_2 ratio (B) for different Ni-containing MCM-41 catalysts at 750 °C for 72 h. Reaction conditions: WHSV (mL/h gCat) = 50,000, $CH_4/CO_2/He$ = 1:1:2, temperature = 750 °C, P = 1 atm.

important factors affecting the catalyst performance. In this study, the spent catalysts after 72 h on stream at 750 °C were characterized by XRD, TGA, Raman spectra, and TEM to get more insights into the factors affecting the deactivation behavior of various Ni-based MCM-41 catalysts.

XRD profiles of the spent catalysts are shown in Fig. 6. The crystal structure and crystalline phases of the spent catalysts are different as compared to the ones observed on fresh catalysts. Part of the amorphous silica matrix of 2Ni–1Ti and 2Ni–1Mn catalysts has been transformed into stable SiO_2 phases, namely, quartz and/or tridymite, especially for 2Ni–1Ti catalyst. This solid phase transformation of the MCM-41 support suggests that the incorporation of Ti or Mn ions is unfavorable for the thermal stability of MCM-41 silica support under reaction conditions. On the contrary, the introduction of Zr cations stabilizes the MCM-41 silica support. It is clear that no crystalline SiO_2 phase is detected on the spent Ni–

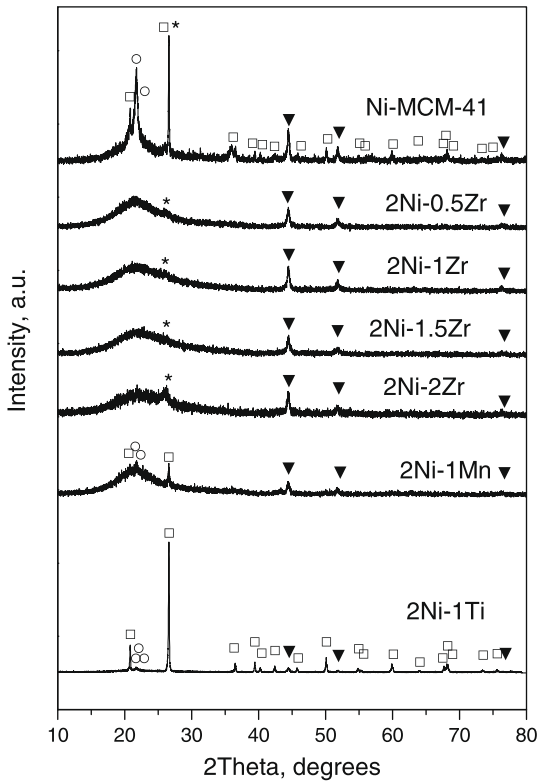

Fig. 6. XRD profiles of spent catalysts after 72 h reaction. (From bottom to top): 2Ni–1Ti, 2Ni–1Mn, 2Ni–2Zr, 2Ni–1.5Zr, 2Ni–1Zr, 2Ni–0.5Zr, and Ni–MCM-41. (Crystalline phase: (1) □, quartz; (2) ○, tridymite; (3) ∗, graphite carbon; (4) ▼, metallic Ni.)

Zr catalysts. Graphitic carbon can be detected for all spent catalysts with the exception of 2Ni–1Mn and 2Ni–1Ti. This is in agreement with the extremely low activity of these samples. All spent catalysts show the presence of metallic Ni. The average particle sizes of Ni particles calculated by Scherrer equation are presented in Table 2. Among the Zr-promoted catalysts and the unpromoted one, the used 2Ni–1Zr sample possesses the smallest particle size (21 nm), whereas the other catalysts show similar particle size (24–26 nm).

The carbonaceous deposit on highly active samples (Ni–MCM-41, Ni–Zr–MCM-41 series) was investigated by performing TG–DTA experiments under oxidative atmosphere (Fig. 7; TG–DTA profiles of 2Ni–1Ti and 2Ni–1Mn samples are also included for comparison). The weight loss is estimated from 110 °C to exclude the interference of moisture. The weight gain arising by Ni oxidation can be neglected due to the low nickel loading. Moreover, due to the similar Ni loading for all catalysts, the weight gain related to Ni oxidation is expected to be the same. As shown in Fig. 7A, the total amount of carbon deposition over the spent catalyst increases in the following sequence: Ni–MCM-41 (4.1%) < 2Ni–0.5Zr (5.0%) < 2Ni–1.5Zr (5.3%) < 2Ni–1Zr (6.0%) < 2Ni–2Zr (7.7%).

An obvious exothermic peak(s) can be observed for all catalysts except for 2Ni–1Ti and 2Ni–1Mn samples in the DTA profiles. These exothermic peaks result from the oxidation/combustion of the carbon species deposited on the catalysts.(Fig. 7B). The presence of a well-defined peak between ca. 500 and 700 °C indicates that the carbon species deposited on the surface of the catalysts exhibit a relatively high degree of graphitization [52]. Two or three kinds of carbon species were identified over Ni catalysts in previous studies [17,49,53,54]. Over spent Ni/SiO_2 catalysts, two peaks at around 350 and above 600 °C, respectively, were observed using TPO [52]. Depending on the removal temperature, three kinds of carbonaceous species were identified over Ni catalysts using O_2-TPSR, designated as C_α (150–220 °C), C_β (530–600 °C), and C_γ (>650 °C) [17]. The prolonged exposure under reaction conditions leads to the increase of the C_β and C_γ species due to their relative inertness. Two distinct exothermic peaks were detected over deactivated Ni/ZrO_2, showing that two different types of carbon species exist [54]. During CH_4 reforming, both CH_4 decomposition and CO disproportionation can be responsible for carbon deposition [49,51].

In summary, based on the TG/DTA results, two different types of carbon species were observed over the spent catalysts investigated in this contribution; namely, easily oxidized carbon and deactivating carbon, corresponding to the temperature range of weight loss of 110–500 and 500–800 °C, respectively, The exothermal peak(s) between 580 and 620 °C observed for all spent catalysts can be attributed to the oxidation of the relatively inert carbon or deactivating carbon species, whereas the weight loss at temperatures lower than 500 °C is ascribed to the easily oxidized carbonaceous deposit. The easily oxidized carbons are preferentially formed during the early stage of reforming, mainly via CH_4 decomposition. The relatively inert carbon species are accumulated with increasing reaction time on stream. This deactivating carbon species come from both reactants, CH_4 and CO_2, since both reacting molecules may lead to the formation of CO and, then, to carbon deposition via Boudaouard reaction [55]. Therefore, when only deactivating carbon is considered, the amount of carbon deposited over the spent catalysts increases in the following sequence: Ni–MCM-41 (3.3%) ~ 2Ni–1.5Zr (3.4%) < 2Ni–0.5Zr (3.6%) < 2Ni–1Zr (4.0%) < 2Ni–2Zr (7.0%).

Raman spectroscopy is a powerful technique to characterize the structure and the compositions of carbonaceous species over spent catalysts [56,57]. Fig. 8 displays the Raman spectra of spent catalysts. All recorded Raman spectra show two major bands at around 1328 cm^{-1} (D band) and 1580 cm^{-1} (G band), respectively, being the intensity of the G band stronger than that of the D band. The D band, also known as the disorder-induced band, is mainly due to structural imperfections, which exist in defective, polycrystalline graphite and other carbonaceous materials [58]; whereas the G band is attributed to graphitic carbon which arises from the in-plane carbon–carbon stretching vibrations of pairs of sp^2 carbons. The broadening or multi-peak features of the G band reflect the symmetry breaking of the tangential vibration, reflecting some rolling in the graphite sheet [59]. The greater intensity of the 1580 cm^{-1} band reveals the presence of more graphitic carbon rather than disordered carbonaceous species over the spent catalysts.

TEM results of selected spent catalysts, Ni–MCM-41, 2Ni–1Zr, 2Ni–1Ti, and 2Ni–1Mn, are shown in Fig. 9. Over the spent 2Ni–1Zr catalyst, most of the Ni particles are between 10 and 20 nm in diameter along with a few larger particles of 35–70 nm; the presence of these small Ni particles validated the stabilization effect of Zr incorporation. On the contrary, there is a considerable amount of Ni particles larger than 50 nm on the Ni–MCM-41 catalyst, suggesting that a significant higher metal sintering occurs during the reaction. No carbon species are found over the spent 2Ni–1Ti and 2Ni–1Mn catalysts, probably due to the strong decoration of Ni-active centers by TiO_x or MnO_x. Much smaller Ni particles (particle size below 10 nm) exist on sample 2Ni–1Ti, whereas the presence of relatively larger particle sizes (20–30 nm) are observed on sample 2Ni–1Mn, partly resulting from the easier reduction of MnO_x species.

A few carbon nano-fibers and multi-walled carbon nanotubes (MWCNTs) have been observed on Zr-incorporated sample (Fig. 9E). Both MWCNTs and other amorphous and graphitic carbons can be detected, in agreement with the Raman results. In addition, small amounts of Ni crystals sitting at the middle or the

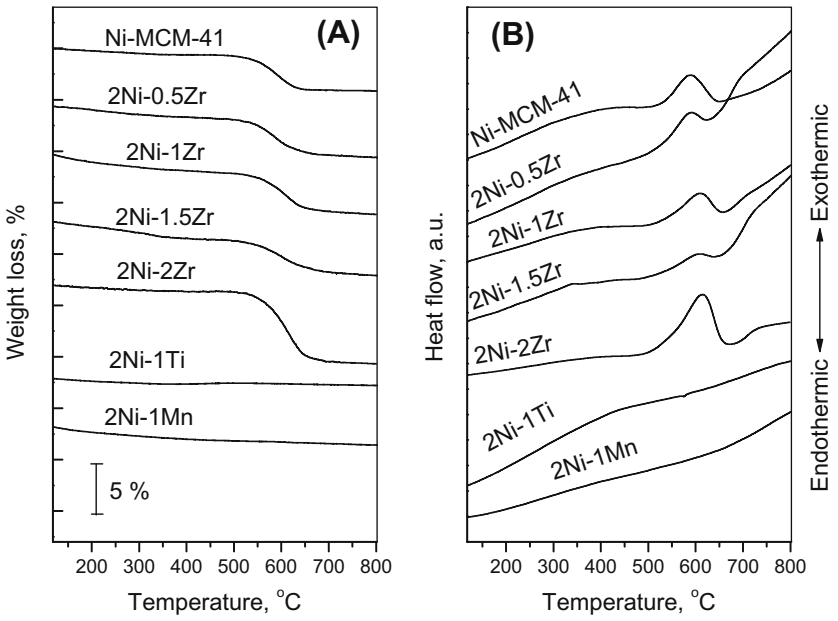

Fig. 7. TG–DTA profiles of representative spent catalysts after 72 h reaction. Ni–MCM-41, 2Ni–0.5Zr, 2Ni–1Zr, 2Ni–1.5Zr, 2Ni–2Zr, 2Ni–1Mn, and 2Ni–1Ti.

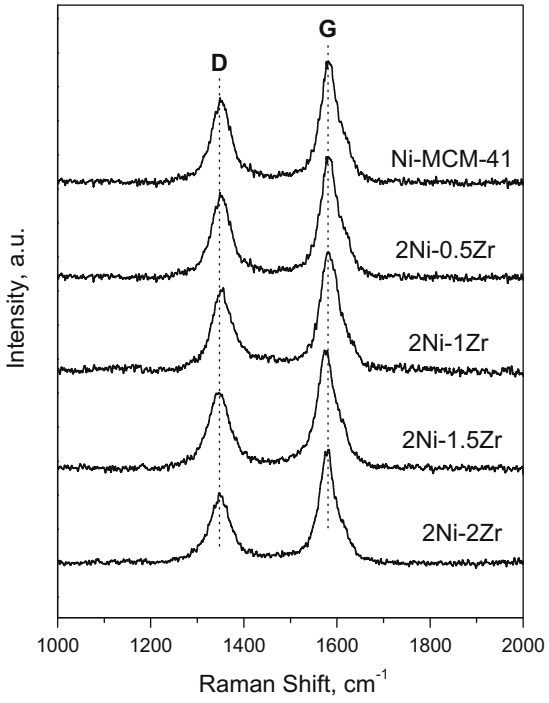

Fig. 8. Raman spectra of carbon deposits over spent catalysts after 72 h reaction.

top of carbon structures, probably due to the detachment and migration of the Ni clusters from the support, can also be observed.

Fig. 10 shows total weight loss caused by carbon deposition, the percentage of different types of carbon as well as initial CH_4, conversion and deactivation rate during stability test as a function of Zr^{4+} nominal loading. It is evident that no clear correlations between carbon deposition and the loading of Zr^{4+} cations incorporated into the silica framework can be established. In general, total amount of carbon deposition increases gradually with the increase of Zr^{4+} loading. Interestingly, a volcano curve exits for the percentages of the two different carbon species. A higher percentage of inert carbon is observed on 2Ni–2Zr and Ni–MCM-41 while the minimum percentage is obtained on sample 2Ni–1Zr. Correspondingly, the lower percentage of easily oxidized carbon is produced on 2Ni–2Zr and Ni–MCM-41 while the higher percentages are found on samples 2Ni–1Zr and 2Ni–1.5Zr. Therefore, the addition of Zr^{4+} seems to decrease the percentage of deactivating carbon. The sudden increases in total amount of carbon deposition and the percentage of inert carbon for this specific sample might be related to the preferential exposure of Ni species and non-intimate contact between metal-active sites and Zr^{4+} species. Regarding the catalytic performance, the initial activity slightly increases while the deactivation rate is significantly suppressed upon Zr^{4+} incorporation, 2Ni–1Zr showing the best catalytic stability. The superior catalytic performance and mild carbon formation of 2Ni–1Zr suggest that an optimum amount of Zr^{4+} is required to minimize the formation of inert carbon.

The lower catalytic activity over the Ni–MCM-41 can be further demonstrated comparing the turnover frequency (TOF) of CH_4 (s^{-1}) defined as methane converted per surface Ni atom per second. During stability test at 750 °C, the TOF values of various catalysts show the following sequence: Ni–MCM-41 (0.75) < 2Ni–0.5Zr (0.82) < 2Ni–1Zr ~ 2Ni–1.5Zr (1.1) < 2Ni–2Zr (1.2). These catalytic results reflect the beneficial effect of Zr^{4+} incorporation on the catalytic activity during dry reforming of Ni catalysts. A slight increase of TOF over 2Ni–2Zr is likely due to a larger number of Zr^{4+} species involved in the reaction. However, due to the larger average Ni particle size over 2Ni–2Zr as compared to the Ni particle sizes on other Ni–Zr catalysts, the rate of carbon formation and the accumulation of carbon species and further transformation into the less active carbon are slightly favored. It should be mentioned that the TOF values for the catalysts studied here are comparable to those reported in the literature. Wei et al. also found a higher TOF_{CH_4} value (1.1 s^{-1}) over 5 wt.% Ni/ZrO_2 at 757 °C after 10 h reaction as compared to 5 wt.% Ni/SiO_2 (0.5 s^{-1}), attributing this to the nano-composite nature of Ni–ZrO_2 system [60]. For Ni/MgO catalysts, CH_4 TOF values in the range of 3.8–5.4 s^{-1} were observed at 750 °C under steady state conditions. These higher TOF values can be attributed to a higher density of Ni-active sites in strong interaction with the support [61]. Similar TOF results were also reported for noble metal catalysts. Over 1 wt.% $Pt/ZrO_2/Al_2O_3$ at 550 °C, CH_4 TOF

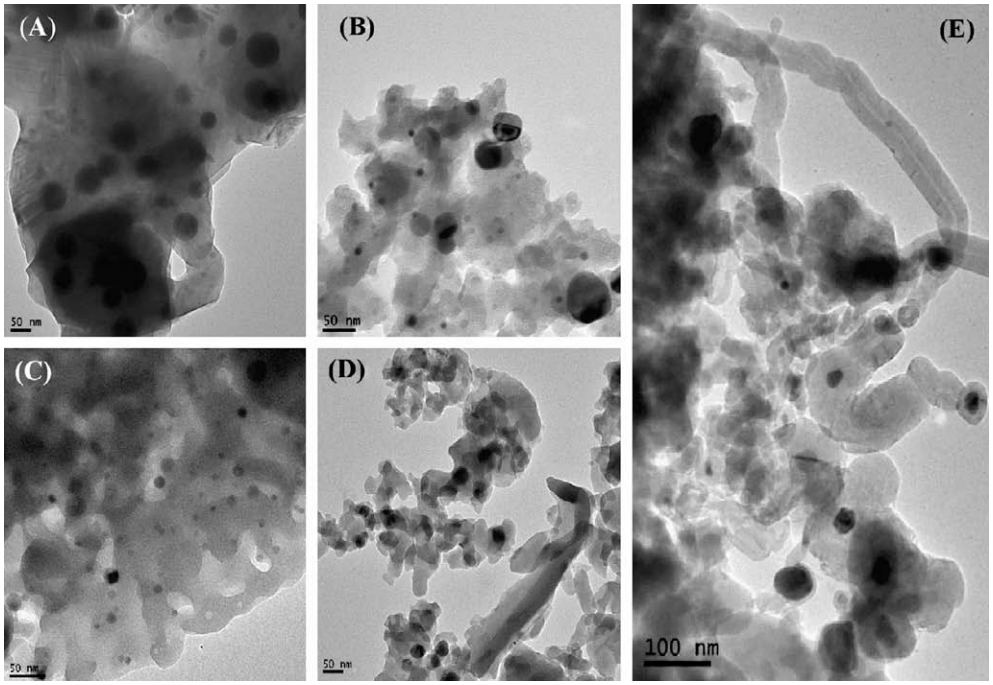

Fig. 9. TEM micrograph of the representative spent catalysts after 72 h reaction: (A) Ni–MCM-41, (B) 2Ni–1Zr, (C) 2Ni–1Ti, (D) 2Ni–1Mn, and (E) 2Ni–1Zr illustrating carbon deposits along with Ni particles.

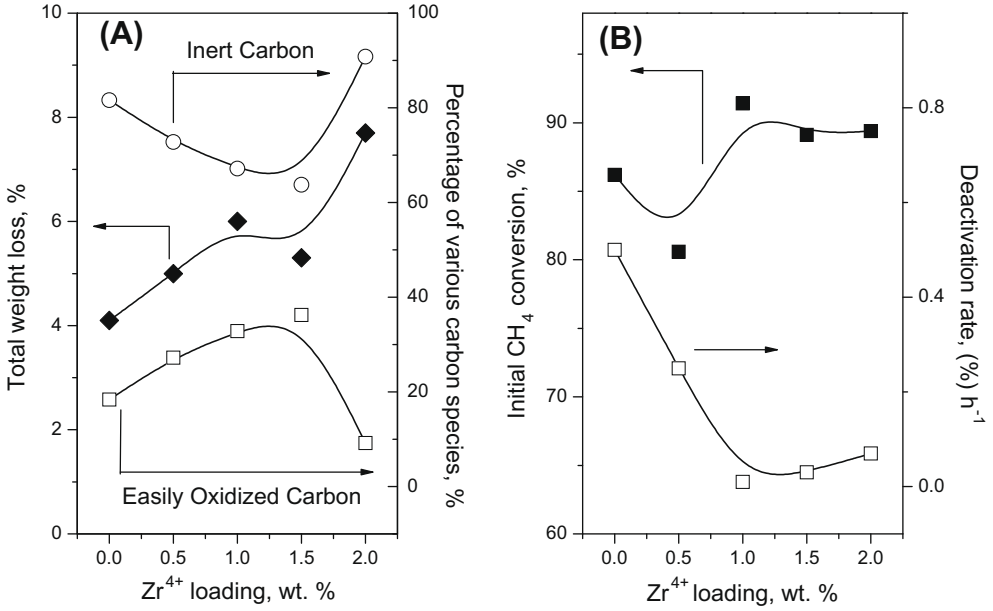

Fig. 10. (A) Weight loss and the percentage of carbon types as a function of Zr^{4+} loading. (B) The initial CH_4 conversion and deactivation rate under stability test as a function of Zr^{4+} loading.

values between 0.77 and 2.2 s^{-1} were found [62]. Using Pt and Rh-based catalysts, CO_2 TOF values between 1.2 and 4.6 s^{-1} were reported, although Rh/ZrO_2 and $Rh/\gamma\text{-}Al_2O_3$ exhibited slightly higher activity than Pt/ZrO_2, showing TOF_{CO_2} values of 4.6 ($Rh/\gamma\text{-}Al_2O_3$), 2.2 (Rh/ZrO_2), and 1.2 s^{-1} (Pt/ZrO_2), respectively [63]. A similar trend is expected for the CH_4 TOF values since similar CH_4 and CO_2 conversions were observed.

In order to explain the higher catalytic stability of Zr-incorporated samples as compared to the Ni–MCM-41 catalyst, it can be speculated that the reactivity of carbon deposits increases with the incorporation of Zr^{4+} species. In addition, a fraction of the relatively inert carbonaceous species may also participate in the reforming reaction besides the easily oxidized carbon species for the Ni–Zr catalysts with higher Zr content. A similar explanation has already been suggested for CaO-promoted Ni/Al_2O_3, ascribing their improved stability to the enhanced reactivity of the less active carbon species, C_β and C_γ species [17]. Park and co-workers also observed that 13% Ni/ZrO_2 catalyst shows the highest activity in spite of the formation of a larger amount of carbon, suggesting the involvement of carbon species as reaction intermediates [64]. Notably, CO_2 can be adsorbed and activated by Zr^{4+} species at the Ni–Zr boundaries in Ni–Zr catalysts, which further oxidizes the

active carbon species formed from CH_4 dissociation on the metal particles, therefore enhancing the catalytic activity due to the presence of boundary sites between Ni particles and Zr species. A similar activation effect was also found on Ni/ZrO_2 [21] and Pt/ZrO_2 catalysts [65]. Their enhanced catalytic performance mainly depends on the presence of high concentration of metal–ZrO_2 interphases. FT-IR spectroscopy of CO_2 adsorption on Pt catalysts indicates the formation of linearly bound CO on Pt and carbonate type species on ZrO_2, while no carbonate species are detected on SiO_2 support [65]. In contrast to the active centers on Zr-incorporated samples, the metal particles on Ni–MCM-41 catalysts can be easily sintered under severe reaction conditions. In addition, the collapse of the MCM-41 structure, as clearly indicated by the formation of crystalline phases of SiO_2 on the XRD patterns, can strongly deactivate the catalysts. This is mainly because some of the Ni-active sites are no longer accessible. By introducing Zr^{4+} into the silica matrix, significant improvement of metal dispersion, structural stability, long-term catalytic stability, and lower deactivation rate are observed (see Table 2, Figs. 6 and 8). The highest stability of 2Ni–1Zr coincides with the smallest crystal size of Ni particles, suggesting an optimal Zr^{4+} loading is required to stabilize small Ni particles. Similar to the anchoring effect reported by Yang et al. [47] and Lim et al. [66] over Ni–MCM-41 and Co–MCM-41 catalysts, respectively, the higher catalytic activity and stability of Zr-incorporated catalysts can be associated with the anchoring of small metallic clusters by un-reduced or partially reduced metal cations located within the silica framework. Noticeably, the anchoring effect in Ni–Zr catalysts is remarkably stronger than that provided by Ni^{2+} or the silica matrix of Ni–MCM-41 due to the presence of irreducible Zr^{4+} cations in the MCM-41 silica framework. In summary, the higher catalytic stability over the Ni–Zr series could be ascribed to the higher structural stability, the stronger anchoring effect of Zr^{4+} as well as to the unique CO_2 activation properties of Zr^{4+} ions.

4. Conclusions

Ni-based bimetallic catalysts supported on MCM-41 silica were prepared by a direct hydrothermal method. XRD patterns and nitrogen physisorption confirmed the existence of ordered mesoporous silica. High metal dispersions were obtained with the incorporation of Zr cations, while remarkably low dispersions were obtained on Ti- or Mn-incorporated samples. These catalysts showed different catalytic activity and stability in methane reforming with CO_2. The catalytic activity of 2Ni–1Mn and 2Ni–1Ti catalysts was significantly lower than that of Ni–MCM-41. On the contrary, all Ni–Zr series catalysts exhibited comparable or enhanced initial catalytic activities. No significant deactivation was found during the stability test over the Ni–Zr catalysts with 2 wt.% Ni and 1–2 wt.% Zr. This high stability was attributed to the improved thermal stability of the MCM-41 structure, the formation of well-dispersed Ni particles due to the anchoring effect of Zr^{4+} species as well as of the ability of Zr^{4+} species to activate CO_2. On the contrary, the negative effect observed on Ti- and Mn-incorporated samples was probably caused by the encapsulation or coverage of Ni-active sites by partially reduced TiO_x and MnO_x species. The low structural stability on Ni–Ti and Ni–Mn catalysts also plays an important role on the catalyst deactivation

Acknowledgments

The authors thank AcRF tier 1 (RG 45/06) and AcRF tier 2 (M45120006 ARC 13/07) for providing funding support. The financial support of A*STAR project 062 101 0035 is gratefully acknowledged.

References

[1] J.R.H. Ross, A.N.J. van Keulen, M.E.S. Hegarty, K. Seshan, Catal. Today 30 (1996) 193.
[2] I. Wender, Fuel Process. Technol. 48 (1996) 189.
[3] M. Levy, R. Lvitan, E. Meirovitch, A. Segal, H. Rosin, R. Rubin, Sol. Energy 48 (1992) 395.
[4] S. Wang, G.Q.M. Lu, Energy Fuel 10 (1996) 896.
[5] Y.H. Hu, E. Ruckenstein, Adv. Catal. 48 (2004) 297.
[6] J.R. Rostrup-Nielsen, J.H.B. Hansen, J. Catal. 144 (1993) 38.
[7] A.T. Ashcroft, A.K. Cheetham, M.L.H. Green, P.D.F. Vernon, Nature 352 (1991) 225.
[8] V.C.H. Kroll, H.M. Swaan, C. Mirodatos, J. Catal. 161 (1996) 409.
[9] J.T. Richardson, S.A. Paripatyadar, Appl. Catal. 61 (1990) 293.
[10] A.M. Gadalla, M.E. Sommer, Chem. Eng. Sci. 43 (1988) 3049.
[11] A. Bhattacharyya, V.W. Chang, Stud. Surf. Sci. Catal. 88 (1994) 207.
[12] Y.G. Chen, J. Ren, Catal. Lett. 29 (1994) 39.
[13] D. Lee, P. Hacarlioglu, S.T. Oyama, Top. Catal. 29 (2004) 45.
[14] A.K. Prabhu, A. Liu, L.G. Lovell, S.T. Oyama, J. Membr. Sci. 177 (2000) 83.
[15] J.R. Rostrup-Nielsen, Stud. Surf. Sci. Catal. 81 (1994) 25.
[16] E. Ruckenstein, Y.H. Hu, Appl. Catal. 133 (1995) 149.
[17] Z.L. Zhang, X.E. Verykios, Catal. Today 21 (1994) 589.
[18] A.A. Lemonidou, I.A. Vasalos, Appl. Catal. A 228 (2002) 227.
[19] X.E. Verykios, Int. J. Hydrogen Energy 28 (2003) 1045.
[20] J.A. Lercher, J.H. Bitter, W. Hally, W. Niessen, K. Seshan, Stud. Surf. Sci. Catal. 101 (1996) 463.
[21] J.M. Wei, B.Q. Xu, J.L. Li, Z.X. Cheng, Q.M. Zhu, Appl. Catal. A 196 (2000) L167.
[22] S.-H. Seok, S.H. Han, J.S. Lee, Appl. Catal. A 215 (2001) 31.
[23] J.B. Wang, L.-E. Kuo, T.-J. Huang, Appl. Catal. A 249 (2003) 93.
[24] J.G. Zhang, H. Wang, A.K. Dalai, J. Catal. 249 (2007) 300.
[25] D. Halliche, R. Bouarab, O. Cherifi, M.M. Bettahar, Catal. Today 29 (1996) 373.
[26] T.C. Xiao, T. Suhartanto, A.P.E. York, J. Sloan, M.L.H. Green, Appl. Catal. A 253 (2003) 225.
[27] J.S. Beck, J.C. Vartuli, W.J. Roth, M.E. Leonowicz, C.T. Kresge, K.D. Schmitt, C.T-W. Chu, D.H. Olson, E.W. Sheppard, S.B. McCullen, J.B. Higgins, J.L. Schlenker, J. Am. Chem. Soc. 114 (1992) 10834.
[28] A. Corma, Chem. Rev. 97 (1997) 2373.
[29] J.C. Vartuli, T.F. Degnan Jr., Stud. Surf. Sci. Catal. 168 (2007) 837.
[30] G.A. Du, S.Y. Lim, Y.H. Yang, C. Wang, L. Pfefferle, G.L. Haller, Appl. Catal. A 302 (2006) 48.
[31] G.A. Du, S.Y. Lim, Y.H. Yang, C. Wang, L. Pfefferle, G.L. Haller, J. Catal. 249 (2007) 370.
[32] D.P. Liu, R. Lau, A. Borgna, Y.H. Yang, Appl. Catal. A 358 (2009) 110.
[33] K.M. Reddy, C. Song, Catal. Lett. 36 (1996) 103.
[34] S. Brunauer, P.H. Emmett, E. Teller, J. Am. Chem. Soc. 60 (1938) 309.
[35] E.P. Barrett, L.G. Joyner, P.P. Halenda, J. Am. Chem. Soc. 73 (1951) 373.
[36] S. Biz, M.L. Occelli, Catal. Rev. Sci. Eng. 40 (1998) 329.
[37] C. Lepetit, M. Che, J. Phys. Chem. 100 (1996) 3137.
[38] B. Scheffer, J.J. Heijeinga, J.A. Moulijn, J. Phys. Chem. 91 (1987) 4752.
[39] L.F. Chen, J.A. Wang, L. Noreña, J. Aguilar, J. Navarrete, P. Salas, J.A. Montoya, P. Del Angel, J. Solid State Chem. 180 (2007) 2958.
[40] D. Trong On, S. Nguyen, V. Hulea, E. Dumitriu, S. Kaliaguine, Micropor. Mesopor. Mater. 57 (2003) 169.
[41] C. Geobaldo, S. Bordiga, A. Zecchina, E. Giamello, Catal. Lett. 16 (1992) 109.
[42] R.K. Jha, S. Shylesh, S.S. Bhoware, A.P. Singh, Micropor. Mesopor. Mater. 95 (2006) 154.
[43] Q. Zhang, Y. Wang, S. Itsuki, T. Shishido, K. Takehira, J. Mol. Catal. A 188 (2002) 189.
[44] S. Velu, N. Shah, T.M. Jyothi, S. Sivasanker, Micropor. Mesopor. Mater. 33 (1999) 61.
[45] A. Derylo-Marczewska, W. Gac, N. Popivnyak, G. Zukocinski, S. Pasieczna, Catal. Today 114 (2006) 293.
[46] Y.H. Yang, S. Lim, G.A. Du, C.A. Wang, D. Ciuparu, Y. Chen, G.L. Haller, J. Phys. Chem. B 110 (2006) 5927.
[47] Y. Yang, S. Lim, G. Du, Y. Chen, D. Ciuparu, G.L. Haller, J. Phys. Chem. B 109 (2005) 13237.
[48] E.P. Reddy, L. Davydov, P.G. Smirniotis, J. Phys. Chem. B 106 (2002) 3394.
[49] M.C.J. Bradford, M.A. Vannice, Appl. Catal. A 142 (1996) 73.
[50] S.J. Tauster, Acc. Chem. Res. 20 (1987) 389.
[51] H.M. Swaan, V.C.H. Kroll, G.A. Martin, C. Mirodatos, Catal. Today 21 (1994) 571.
[52] Zhixin Yu, De Chen, Magnus Rønning, Bård Tøtdal, Torbjørn Vrålstad, Esther Ochoa-Fernández, Anders Holmen, Appl. Catal. A 338 (1–2) (2008) 147.
[53] S.B. Wang, G.Q. Lu, Ind. Eng. Chem. Res. 38 (1999) 2615.
[54] W. Hally, J.H. Bitter, K. Seshan, J.A. Lercher, J.R.H. Ross, Stud. Surf. Sci. Catal. 88 (1994) 167.
[55] V.C.H. Kroll, H.M. Swann, S. Lacombe, C. Mirodatos, J. Catal. 164 (1997) 387.
[56] B.M. Vogellarr, A.D. van Langeveld, S. Eijsbouts, J.A. Moulijn, Fuel 86 (2007) 1122.
[57] D. Espinat, H. Dexpert, E. Freund, G. Martino, Appl. Catal. 16 (1985) 343.
[58] A. Cuesta, P. Dhamelincourt, J. Laureyns, A. Martinez-Alonso, J.M.D. Tascón, Carbon 32 (1994) 1523.
[59] A. Jorio, R. Saito, G. Dresselhaus, M.S. Dresselhaus, Philos. Trans. R. Soc. Lond. A 362 (2004) 2311.

[60] J.M. Wei, B.Q. Xu, J.L. Li, Z.X. Cheng, Q.M. Zhu, in: C.S. Song, A.M. Gaffney, K. Fujimoto (Eds.), CO_2 Conversion and Utilization, ACS Symposium Series, vol. 809, American Chemical Society, Washington, DC, 2002, p. 197.
[61] Y.H. Wang, H.M. Liu, B.Q. Xu, J. Mol. Catal. A 299 (2009) 44.
[62] M.M.V.M. Souza, D.A.G. Aranda, M. Schmal, J. Catal. 204 (2001) 498.
[63] J.H. Bitter, K. Seshan, J.A. Lercher, J. Catal. 176 (1998) 93.
[64] J.-S. Chang, D.-Y. Hong, X.S. Li, S.-E. Park, Catal. Today 115 (2006) 186.
[65] J.H. Bitter, K. Seshan, J.A. Lercher, J. Catal. 171 (1997) 279.
[66] S. Lim, C. Wang, Y. Yang, D. Ciuparu, L. Pfefferle, G.L. Haller, Catal. Today 123 (2007) 122.